Journal of Colloid and Interface Science 686 (2025) 1135–1146

Contents lists available at ScienceDirect

Journal of Colloid And Interface Science

journal homepage: www.elsevier.com/locate/jcis

Regular Article

A coarse-grained model for aqueous two-phase systems: Application to ferrofluids

Alberto Scacchi [a,b,c,*], Carlo Rigoni [b,c,d], Mikko Haataja [e], Jaakko V.I. Timonen [b,c], Maria Sammalkorpi [c,f]

[a] Department of Mechanical and Materials Engineering, University of Turku, Vesilinnantie 5, 20500 Turku, Finland
[b] Department of Applied Physics, Aalto University, Konemiehentie 1, 02150 Espoo, Finland
[c] Academy of Finland Center of Excellence in Life-Inspired Hybrid Materials (LIBER), Aalto University, P.O. Box 16100, FI-00076 Aalto, Finland
[d] Institute of Science and Technology Austria, Am Campus 1, 3400 Klosterneuburg, Austria
[e] Department of Mechanical and Aerospace Engineering, and Princeton Materials Institute (PMI), Princeton University, Princeton, NJ 08544, United States
[f] Department of Chemistry and Materials Science, Aalto University, P.O. Box 16100, FI-00076 Aalto, Finland

GRAPHICAL ABSTRACT

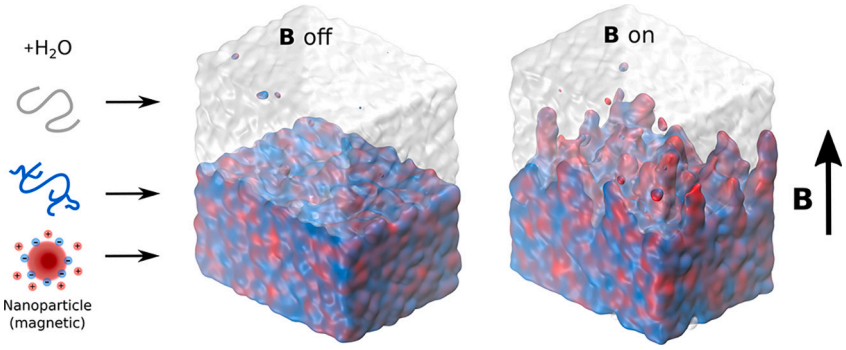

ARTICLE INFO

Dataset link: https://doi.org/10.23729/4fb80194-cdb2-4f49-94f4-f8a87b8e29c1

Keywords:
Polymeric aqueous two-phase systems
Coarse-grained model
Phase separation
Partitioning
Liquid-liquid interface
Surface tension
Magnetic response
Pattern formation

ABSTRACT

Aqueous two-phase systems (ATPSs), phase-separating solutions of water soluble but mutually immiscible molecular species, offer fascinating prospects for selective partitioning, purification, and extraction. Here, we formulate a general Brownian dynamics based coarse-grained simulation model for an ATPS of two water soluble but mutually immiscible polymer species. Including additional solute species into the model is straightforward, which enables capturing the assembly and partitioning response of, e.g., nanoparticles (NPs), additional macromolecular species, or impurities in the ATPS. We demonstrate that the simulation model captures satisfactorily the phase separation, partitioning, and interfacial properties of an actual ATPS using a model ATPS in which a polymer mixture of dextran and polyethylene glycol (PEG) phase separates, and magnetic NPs selectively partition into one of the two polymeric phases. Phase separation and NP partitioning are characterized both via the computational model and experimentally, under different conditions. The simulation model captures the trends observed in the experimental system and quantitatively links the partitioning behavior to the component species interactions. Finally, the simulation model reveals that the ATPS interface fluctuations in systems with magnetic NPs as a partitioned species can be controlled by the magnetic field at length scales much smaller than those probed experimentally to date.

* Corresponding author.
E-mail address: alberto.scacchi@utu.fi (A. Scacchi).

https://doi.org/10.1016/j.jcis.2025.01.256
Received 14 October 2024; Received in revised form 29 January 2025; Accepted 29 January 2025

Available online 31 January 2025

1. Introduction

Phase separation of macromolecular solutions into coexisting aqueous phases underlies the formation of membraneless compartments in biological cells [1–4], gives rise to advanced functionalities in polymeric materials [5], and enables a broad range of technological applications related to biomolecules and bio species, including separation and purification of nucleic acids and proteins (enzymes and antibodies), as well as extraction of viruses [6–8]. Furthermore, aqueous phase-separating solutions also hold the promise for low environmental impact extraction techniques [9] and find broad usage in biomedicine and biopharmaceuticals [10,11], as well as in biotechnology [6,12,13]. Phase-separating systems can also guide cellular micropatterning and encapsulation to mimic biological cells [14]. Also several pathological conditions, including those associated with neurological diseases [15] or cancer spreading [16], may be affected by phase-separation.

At a general level, aqueous two-phase systems (ATPSs) form when incompatible polymers and/or salts are mixed with water such that coexisting phases each enriched in one of the two components rise in the solution [17,18]. In a prior work, we examined a polymer-based ATPS experimentally, in the context of a ferrofluid system [19]. Ferrofluids, colloidal suspensions of magnetic nanoparticles in fluids, allow external field driven reversible pattern formation [20]. Their magnetically [21–24] and electrically [25] driven control enable a variety of advanced technological applications [20,26,27]. The magnetically responsive NPs in polymer solutions also have broad use in biomedical technologies, e.g., with various drug delivery [28], including targeted thermochemotherapy [29] approaches. The enhanced thermal conductivity of NP based ferrofluids also enables energy storage and energy generation applications [26,30].

Characteristic to ferrofluid systems is their pattern formation via magnetic field induced instabilities. Well-known instabilities include, e.g., the normal-field or Rosensweig [31] and the labyrinthine patterns [32–34]. The former is also observed in magnetic Bose Einstein condensates [35] but also in dissipative electrodriven gradients of NPs [25]. The pattern periodicity in these increases proportionally with the square root of the interfacial tension [36]. In an ATPS, pattern periodicities as small as 100 μm or less can be achieved [19].

Since phase separation of polymer mixtures commonly involves length scales larger than micrometers and characteristic time scales exceeding microseconds, theoretical and computational approaches addressing the phase separation response require coarse-graining of the molecular level details. Typical coarse-grained particle-based modeling approaches for polymer systems at phase separation level include, e.g., dissipative particle dynamics [37] and Brownian or Langevin dynamics simulations [38,39]. Free energy-based field-theoretic approaches include, e.g., self-consistent field theory [40,41], classical density functional theory [42,43], and power functional theory [44]. However, developing predictive field-based approaches is challenging for complex systems. Additionally, field-based approaches typically provide only expectation values and distributions, rather than localized, particle or molecule level information.

In this work, we combine theoretical/simulational and experimental methods to study a polymer-based ATPS. Specifically, we examine the phase separation response via the polymer species and magnetic NP partitioning in the ATPS, and the response of the system to external magnetic field. We formulate here a Brownian dynamics (BD) based general simulation model to describe an ATPS and systematically connect and compare the model to an ATPS introduced and experimentally characterized by us in Ref. 19. Notably, the here developed coarse-grained, particle-based approach that is based on the BD modeling method accesses the required time and length scales to capture the ATPS partitioning and dynamics in the system. It can predict the response of ATPSs, as demonstrated by the comparison between simulated and experimentally measured phase separation and partitioning response for systems of varying characteristics. Throughout, the model construction, verification steps, and the parametrization are presented such that adaptation to other ATPS systems is readily approachable.

2. Materials and methods

2.1. Simulation model and software

Here, a BD simulation model for aqueous solution of two polymers and magnetic NPs is formulated. BD is an implicit-solvent particle-based modeling method [39,45]. The solutes are modeled as particles which are considered to be large in comparison to the solvent molecules (e.g. a polymer molecule vs a single water molecule) [39,45]. The effects rising from the solvent on the solutes are captured via an effective random force term [39]. The approach leads to a computationally very efficient, yet effective in capturing the solvent effects, model for solute dynamics in solutions. Notably, extensive length and time scales in modeling compared to, e.g., atomistic, or even coarse-grained explicit solvent modeling approaches can be captured [38].

In BD, the position vectors $\mathbf{r}_i$ of the particle i at time t

$$\mathbf{r}_i(t+dt) = \mathbf{r}_i(t) - \frac{\nabla\Phi(\mathbf{r}_i,t)}{\Gamma_t}dt + \delta\mathbf{r}_i \tag{1}$$

provide the equations of motion leading to the time evolution of the system via numerical integration with discrete time steps dt. Here, Φ is the total interaction potential, Γ_t the translational friction coefficient, and $\delta\mathbf{r}_i$ models stochastic position changes due to the solvent. Here, Φ includes all the one- and two-body interaction contributions to the solute interactions (see Section 3) and Γ_t is set to be the same for all particles in this work. All interaction potentials are truncated and shifted to zero at different cutoff distances, which are chosen in such way to produce negligible changes. The three components of the stochastic position change $\delta\mathbf{r}_i$ are sampled from a Gaussian distribution with standard deviation $\sqrt{2D_t dt}$. In this, D_t is the translational diffusion constant, which follows the Einstein relation $D_t = k_B T/\Gamma_t$. Here, k_B is the Boltzmann constant and T the temperature. The energy scale is defined by $\beta^{-1} = k_B T$, and is set to 1 in this work. Without loss of generality, we also set $D_t = 1$; this choice sets the time scale of the simulations, and can be used to convert the modeling time scales to their real-time equivalents.

The NPs also have magnetic dipole moments $\boldsymbol{\mu}_i$ that evolve in time following

$$\boldsymbol{\mu}_i(t+dt) = \frac{\boldsymbol{\mu}_i(t) + \boldsymbol{\omega}_i \times \boldsymbol{\mu}_i dt}{|\boldsymbol{\mu}_i(t) + \boldsymbol{\omega}_i \times \boldsymbol{\mu}_i|}, \tag{2}$$

where

$$\boldsymbol{\omega}_i = \frac{\mathbf{T}_i}{\Gamma_r} + \sqrt{2D_r}\frac{d\mathbf{W}}{dt}. \tag{3}$$

In this, $d\mathbf{W}$ is a vector of three uncorrelated random numbers with zero mean and variance dt [46], and D_r is the rotational diffusion constant. It is connected to the corresponding rotational friction coefficient Γ_r by the Einstein relation $D_r = k_B T/\Gamma_r$, reflecting a Boltzmann distribution of orientations and the moments associated with rotational diffusion [46]. Note that this corresponds to a Brownian relaxation of the dipole moments, rather than Néel relaxation [36]. At infinite dilution with stick boundary conditions, Γ_t and Γ_r follow the relation $\Gamma_t = 3\Gamma_r/d^2$, where d is the diameter of the particle. Finally, $\mathbf{T}_i$ describes all torques acting on particle i. These arise from dipole-dipole interactions or from interaction with external fields.

BD-type approaches are valid only if the modeled solute particles are much larger than the solvent molecules and if the velocity-velocity

correlation decays on a time scale much smaller than the characteristic time scale of the system, such as self-diffusion time. This limit is often referred to either as overdamped or viscous limit. Notably, both these conditions are satisfied by the ATPS characterized in Ref. 19 (see Supplementary Material (SM)). If the system is not overdamped (at viscous limit), Langevin dynamics [47] is more appropriate than BD as modeling approach.

The Large-scale Atomic/Molecular Massively Parallel Simulator (LAMMPS) [48] *23 Jun 2022* stable version with an optimized interaction scheme [49,50] was used for the simulations. The initial configurations were prepared using Packmol [51] and Moltemplate [52]. The visualizations were produced using either VMD [53] or Ovito [54].

2.2. Materials and experimental characterization

The mixtures of NPs, PEG, and dextran in water solution were prepared using the following procedure consisting of four steps. First, two separate concentrated solutions of PEG (polyethylene glycol 35000, ≥ 99.9%, 81310, Sigma-Aldrich) and dextran (Dextran T500, ∼ 95%, 40030, Pharmacosmos) were obtained by mixing 75.0 g of polymers with 150.0 g of deionized water (Ultrapure type 1 water obtained with Millipore Direct-Q 3UV). The final densities of the PEG and dextran solutions, measured as in Ref. 19, were 1.052 ± 0.003 g/ml and 1.078 ± 0.001 g/ml, respectively. Second, the main ATPS dispersion was prepared by mixing 2635.2 mg of PEG concentrated solution, 5832.7 mg of dextran concentrated solution, and 20794.7 mg of deionized water. Third, in order to obtain approximately similar final concentrations of iron oxide NPs in all samples, the stock NPs dispersions were diluted using a micropipette (Eppendorf Research Plus) as follows: 15 µl of stock solution of citrate-coated iron oxide NPs (see synthesis details in Ref. 19) + 985 µl of deionized water, 238 µl of phospholipid coated iron oxide NPs (45-111-701, Micromod) + 762 µl of deionized water, 6 µl of pegylated iron oxide NPs (PBG 300, Ferrotec) + 994 µl of deionized water. Finally, the NPs-PEG-dextran dispersions were prepared using the following methodology: the main ATPS dispersion was shaken in order to obtain an unstable emulsion from which, immediately after shaking, 650 µl were collected using a micropipette, and poured in the final container. This step was necessary to ensure that all collected aliquots had the same composition. Similarly the diluted NPs dispersions were shaken, and 100 µl were then collected with a micropipette and poured in the final container. An additional control ATPS was obtained by adding 100 µl of deionized water instead of the NP dispersion. All dispersions were prepared in duplicates in glass vials (Supelco 29403-U) for the photographs and in poly(methyl methacrylate) (PMMA) cuvettes (VWR Cuvettes PMMA semi-micro 634-0678) for the spectrophotometry experiments. All dispersions were then mixed and allowed to equilibrate for 48 hours prior to performing the experiments and obtaining the images, which were collected using a Nikon digital camera D5500. Optical absorption of the samples was measured using a spectrophotometer (Thermo Scientific GENESYS 30). The PMMA cuvettes filled with the samples were placed at different height inside the spectrophotometer to probe the light absorption as a function of the wavelength in both the dilute and dense phases.

3. Results and discussion

3.1. ATPS computational model construction and partitioning results

The construction of the simulation model is presented next in modular steps. First, (1) a binary polymer mixture that exhibits phase separation is considered. Next, (2) a third (magnetically responsive) component that interacts asymmetrically with the two polymer species is introduced. After this, the effects of (3) gravity-like conditions and (4) external magnetic field are examined.

Polymer mixture

To construct the ATPS model, two different polymer species in an implicit aqueous solution are considered. A pair interaction potential for the interactions of the polymer species is needed for the BD equations of motion, Eq. (1). Gaussian-like potentials between centers of mass have been found to describe the effective interaction between both linear polymers and dendrimers in good solvents [55–60]. Because of this, we describe the polymer-polymer interactions via

$$\phi_{ij}(r) = \varepsilon_{ij} e^{-r^2/R_{ij}^2}, \quad i,j = 1,2. \tag{4}$$

Here $r = |\mathbf{r}| = |\mathbf{r}_i - \mathbf{r}_j|$ is the center of mass separation, R_{ij} are proportional to the radius of gyration, and ε_{ij} define the (repulsive) interaction strengths. The sub-indices i and j refer to the species type.

The ATPS comparison system of Ref. 19 polymer components are PEG ("P_1") and dextran ("P_2"), in water. PEG is a linear polymer for which water is a good solvent. Thus, setting $\varepsilon_{11} = 2k_BT$ is well motivated. On the other hand, dextran is a branched polymer for which water is rather a θ-solvent, resulting in dextran coiling [61]. For simplicity, $\varepsilon_{22} = 2k_BT$ also for dextran in the current work despite its branched nature. To the best of our knowledge, a generic functional form of the effective interaction between branched polymers in θ-solvent does not exist.

For the polymer sizes, we set $R_{11} = R_{12} = R_{22} = R$. Notably, in Ref. 19 the radius of gyration of dextran is about twice that of PEG. The remaining variable ε_{12}, which controls the miscibility of the polymers, is unknown for the experimental reference system of Ref. [19]. However, as the reference system is an ATPS, phase separation of the two polymer species is expected.

The condition for phase separation of two polymeric species interacting following Eq. (4) at fixed volume is [62]

$$\chi = \beta\pi^{3/2}\left[2\varepsilon_{12}R_{12}^3 - \left(\varepsilon_{11}R_{11}^3 + \varepsilon_{22}R_{22}^3\right)\right] > 0. \tag{5}$$

Here, χ is a parameter measuring mixing. The instability criterion of our model actually connects with the well known Flory-Huggins theory [63]. The Flory-Huggins theory is a lattice based theory for polymer solvation. A free energy based on polymer chain conformations entropy and interactions energy with the polymer monomers each occupying one lattice site is considered. Considering the Gaussian core model employed in this work, the interaction parameters ε_{ij} would need to model an infinite penalty for overlap to correspond to the Flory-Huggins lattice packing. This restricts direct comparison of the models. However, the phase separation and instability responses of the two models offer interesting connections. Namely, within the Flory-Huggins theory, phase separation occurs when $\chi_{FH} > \chi_{FH}^c = \frac{1}{2}\left(\frac{1}{\varphi_1 L_1} + \frac{1}{(1-\varphi_1)L_2}\right)$, where L_1 and L_2 correspond to the degree of polymerization of the two polymers, φ_1 is the volume fraction of P1 and correspondingly, for a filled lattice, P2 has a volume fraction $\varphi_2 = 1 - \varphi_1$. The parameter χ_{FH}^c is the critical Flory-Huggins mixing parameter. The radius of gyration of a polymer is known to scale as L^ν, where ν depends on the solvent conditions and its value is typically between 1/3 and 3/5 [63]. As the lower limit corresponds to bad solvent, the Flory-Huggins critical mixing parameter $\chi_{FH}^c \propto \left(\frac{R_{g,1}^3}{\varphi_1} + \frac{R_{g,2}^3}{1-\varphi_1}\right)$ in bad solvent conditions. Correspondingly, $\chi_{FH}^c \propto \left(\frac{R_{g,1}^{5/3}}{\varphi_1} + \frac{R_{g,2}^{5/3}}{1-\varphi_1}\right)$ in ideal solvent conditions. This reveals that the size scaling of polymers in solvent clearly has a connection with the instability criterion of the Gaussian core model presented as Eq. (5) here.

Back to our model, we consider the fraction of P_2 polymers $\xi = N_2/N_{tot}$, where N_2 is the number of P_2 polymers and $N_{tot} = N_1 + N_2$ the total number of polymers in the system, the density along the spinodal $\rho_s(\xi)$ in mean field theory at fixed volume, which provides the conditions for instability, is given by [62]

$$\rho_s(\xi) = \left[\xi(1-\xi)\chi\right]^{-1}. \tag{6}$$

Journal of Colloid And Interface Science 686 (2025) 1135–1146

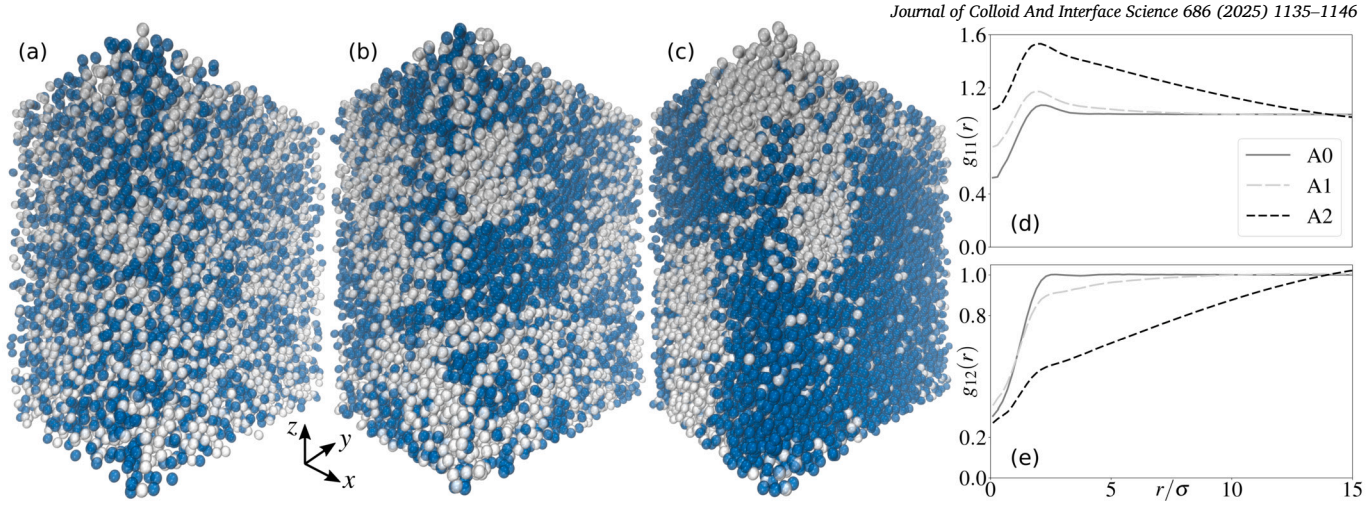

Fig. 1. Assembly configurations in polymer - polymer systems at different concentrations, and the corresponding homogeneous and isotropic radial distribution functions, respectively. Panels correspond to visualizations of the assembly structure in systems (a) A0, (b) A1, and (c) A2 after 200×10^6 time steps. P_1 are gray and P_2 blue. Panels (d) and (e) show the radial distribution functions g_{11} and g_{12}, see Eq. (7). (For interpretation of the colors in the figure(s), the reader is referred to the web version of this article.)

Table I
Summary of the different systems considered in the present work. The columns correspond to the total number of polymers $N_{\rm tot}$, number of nanoparticles $N_{\rm NP}$, total polymer number density $\rho_{\rm tot}\sigma^3$, total nanoparticles number density $\rho_{\rm NP}\sigma^3$, and attraction strength between P_2 and NPs $\beta\varepsilon_{23}$.

System	$N_{\rm tot}$	$N_{\rm NP}$	$\rho_{\rm tot}\sigma^3$	$\rho_{\rm NP}\sigma^3$	$\beta\varepsilon_{23}$
A0	12000	-	0.222	-	-
A1	20000	-	0.370	-	-
A2	25000	-	0.463	-	-
A3	30000	-	0.556	-	-
B1	20000	5000	0.370	0.093	1
B2	20000	5000	0.370	0.093	3
B3	20000	5000	0.370	0.093	4
C1	25000	5000	0.463	0.093	1
C2	25000	5000	0.463	0.093	2
C3	25000	5000	0.463	0.093	3

With the interaction choices made for P_1 and P_2 in the present work, the phase separation criterion $\chi>0$ in Eq. (5) becomes $\varepsilon_{12}>2k_{\rm B}T$. To satisfy this, we choose $\varepsilon_{12}=2.5k_{\rm B}T$.

A thorough study on the mixing and phase separation response under different polymer interaction conditions, ε_{ij} and R_{ij}, is presented in Ref. 64. The choice of setting $R_{ij}=R\quad\forall i,j$ results in the most symmetric phase response (see Fig. 5 in Ref. 64), and enables controlling the partitioning of the NPs solely through the affinity differences.

For the simulations, Eq. (4) is truncated and shifted to zero at separation $r=3.5\sigma$, at which approximately 0.2% of the repulsion magnitude ε_{ij} remains. Here, $\sigma=R/\sqrt{2}$ defines the length scale of the simulations, which is a good approximation for the radius of gyration in the semi-dilute regime of polymer solutions [62]. The simulation volume is $V=L_x\times L_y\times L_z=30\sigma\times40\sigma\times45\sigma$. The critical number of polymers for phase separation to occur, obtained from Eq. (6), is $N_{\rm c}=\rho_{\rm s}V$. For $\xi=0.5$, i.e., $N_1=N_2$, this corresponds to $N_{\rm c}\simeq13715$ in the simulation volume. Converted to number density this is $\rho_{\rm s}\sigma^3\approx0.254$. The effect of polymer concentration changes is examined via comparison of system A0 ($N_{\rm tot}=12000<N_{\rm c}$), system A1 ($N_{\rm tot}=20000>N_{\rm c}$), and system A2 ($N_{\rm tot}=25000>N_{\rm c}$). The examined systems correspond to number densities $\rho_{\rm tot}\sigma^3\approx0.222$, 0.370, and 0.463, respectively. The different system parameters are summarized in Table I.

The experimental comparison system of Ref. 19 contains in the characterized *Sample 0* approximately 19850 polymers in a volume corresponding to the simulation box size (estimated using $\sigma=10$ nm based on the magnitude of the average size of the three solute components in the experiments). The component concentrations lead to an estimate that 2630 of these are dextran and 17220 are PEG. The polymer number count corresponds to a total number density $\rho_{\rm tot}^{\rm exp}\sigma^3\approx0.368$, to which dextran contributes 0.049 and PEG 0.319. Additional details of the estimation are provided in the SM. It is important to note that the lack of gravitational effects in these simulations demonstrates that the phase separation is driven purely by interparticle interactions.

A random mixture of the polymer particles with given particle number densities is used as initial configuration for all simulations. Periodic boundary conditions along the xy plane and reflective hard walls in the z direction are employed. The hard walls in the z direction are expected to slightly affect the bulk phase response, as well as the critical density $\rho_{\rm s}$. The boundaries in the z direction facilitate the study of more realistic systems in which gravity-like conditions are also considered.

Figure 1 displays visualizations of late-time configurations of systems A0, A1, and A2, as well as the corresponding homogeneous and isotropic radial distribution functions [65]

$$g_{ij}(r)=\frac{\rho_j(r,r+dr)}{\rho_j}=\frac{N_{ij}(r,r+dr)}{4\pi\rho_j r^2dr},\tag{7}$$

where N_{ij} is the number of j-type particles found at a distance between r and $r+dr$ (dr small) from an i-type particle. Note that calculating the isotropic RDFs in a slab geometry can produce artifacts, such as the absence of asymptotic convergence to 1 for large values of r, and may also alter the shape of the first coordination shells. Nevertheless, with this data we target for a confirmation of the occurrence of phase separation, which is not affected by the artifacts just discussed. Configurational snapshots in Fig. 1 correspond to simulation time of $200\times10^6\,dt$, where $dt=10^{-5}\tau$. Here, $\tau=\sigma^2/D_{\rm t}$ defines the simulation time scale. All radial distribution functions are calculated considering all particles in the system and over a time period corresponding to the last 10% of the simulation time.

As expected based on Eq. (5), phase separation is observed in systems A1 and A2. The system A2 is deeper within the spinodal region, resulting in significantly different coexisting densities than in A1 and stronger phase separation response. On the other hand, in A0, the polymer concentration is below the critical concentration, and phase separation is not observed.

The visual observations response is confirmed by the radial distribution function data of Fig. 1. Phase separation is indicated by the slow decay of $g_{11}(r)$ evident for A2 but also visible for A1, panel (d), and $g_{22}(r)$ shows the same trend because of symmetry reasons. For the sys-

Journal of Colloid And Interface Science 686 (2025) 1135–1146

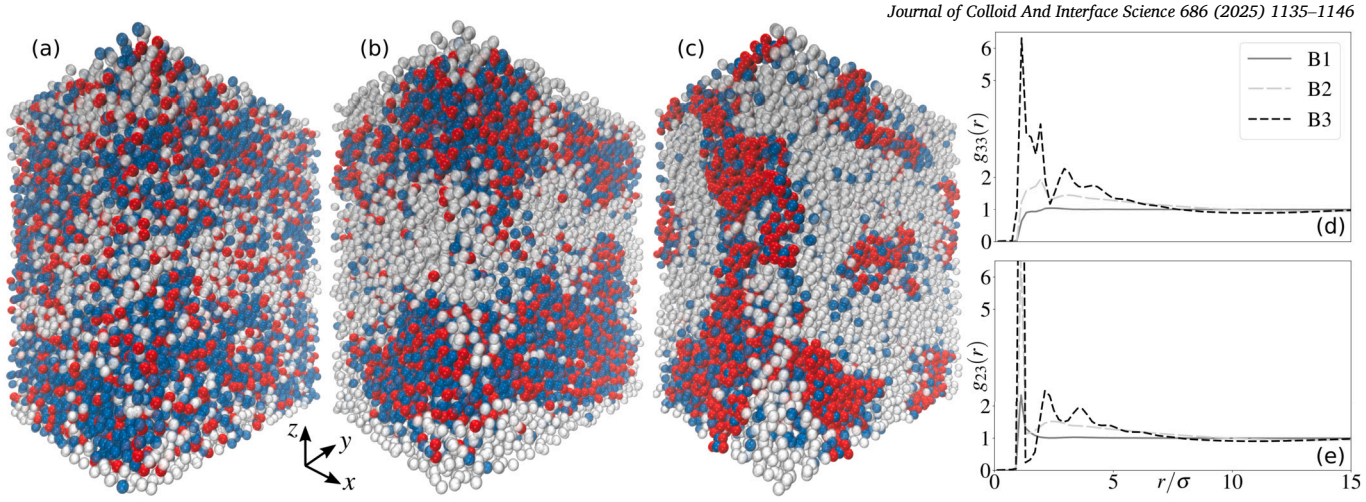

Fig. 2. Assembly configurations rising in modeling polymer - polymer - NP systems with different $\beta\varepsilon_{23}$ values, and the corresponding homogeneous and isotropic radial distribution functions for the third species and its affinity polymer. Panels correspond to visualizations of the assembly structure in system (a) B1 ($\beta\varepsilon_{23}=1$), (b) B2 ($\beta\varepsilon_{23}=2$), and (c) B3 ($\beta\varepsilon_{23}=4$) after 50×10^6 time steps. The value of $\beta\varepsilon_{23}$ indicates attraction strengths between P_2 and the NPs. P_1 are gray, P_2 blue, and NPs red. Panels (d) and (e) show the radial distribution functions g_{33} and g_{23}, see Eq. (7).

tem A0, $g_{11}(r)$ approaches unity with increasing distance r much faster, as expected. The interspecies radial distribution function $g_{12}(r)$ of panel (e) also shows features that are consistent with phase-separation occurring in both A1 and A2: same species particles are condensed and the other species particles depleted at short-range and intermediate distances r.

Polymer mixture with nanoparticles

Let us next introduce a third solute component into the polymer mixture. Generally, this component can represent, besides additional polymer species, e.g., biological macromolecules, such as nucleic acids or proteins, including enzymes and antibodies, virus particles and pathogenic species, as well as colloidal particles – basically anything comparable in size to P_1 and P_2 dispersed in the same aqueous solution. For simplicity, a single additional species is introduced, however, the presented approach and its formulation are not restricted to any specific number of additional components. Motivated by our recent experimental work on ferrofluids [19], the third component consists of magnetic NPs.

The pairwise interactions between the NP species for Eq. (1) are modeled by $\phi_{33}^{\mathrm{tot}}=\phi_{\mathrm{E}}+\phi_{\mathrm{WCA}}+\phi_{\mathrm{D}}$. Here, and in the following, the subindex 3 refers to the NP species, ϕ_{E} captures the electrostatic, ϕ_{WCA} the species dimensions, and ϕ_{D} the dipole-dipole interactions. Following Refs. 19,66, the NPs are assumed to carry some charge and their screened electrostatic interactions are described by

$$\phi_{\mathrm{E}}(r)=\frac{A}{\kappa}e^{-\kappa(r-\sigma_3)}, \tag{8}$$

which corresponds to the interaction between colloids in an electrolyte [67]. In this, $A>0$ controls the strength of the repulsive interactions, κ is the inverse screening length, and σ_3 sets the diameter of the NPs. For simplicity, we set $\sigma_3=\sigma$. The simulations employ $\beta\sigma A=25$ and $\sigma\kappa=5$, which leads to a stable dispersion response for the NPs in an aqueous solution (colloidal behavior; dipole-dipole self-assembly is avoided). In the simulations, ϕ_{E} is truncated and shifted (by approximately $10^{-9}A/\kappa$) to zero at $r=5\sigma$. The standard Weeks-Chandler-Andersen (WCA) potential [68]

$$\phi_{\mathrm{WCA}}(r)=4\varepsilon_3\left[\left(\frac{\sigma}{r}\right)^{12}-\left(\frac{\sigma}{r}\right)^{6}\right]+\varepsilon_3,\quad r<2^{\frac{1}{6}}\sigma, \tag{9}$$

where $\varepsilon_3=1$ is used to prevent the steric overlap of the NPs. The dipole-dipole interactions are modeled by the "shifted-force" dipole-dipole interaction [69]

$$\phi_{\mathrm{D}}(\mathbf{r},\boldsymbol{\mu}_i,\boldsymbol{\mu}_j)=\left[1-4\left(\frac{r}{r_{\mathrm{D}}^{\mathrm{c}}}\right)^3+3\left(\frac{r}{r_{\mathrm{D}}^{\mathrm{c}}}\right)^4\right]\times\left[\frac{1}{r^3}(\boldsymbol{\mu}_i\cdot\boldsymbol{\mu}_j)-\frac{3}{r^5}(\boldsymbol{\mu}_i\cdot\mathbf{r})(\boldsymbol{\mu}_j\cdot\mathbf{r})\right]. \tag{10}$$

In this, $r=|\mathbf{r}|=|\mathbf{r}_i-\mathbf{r}_j|$ is the center-to-center distance of a pair of NPs, and $\boldsymbol{\mu}_i$ and $\boldsymbol{\mu}_j$ are their dipole moment vectors. ϕ_{D} is the computationally most demanding interaction potential and it is truncated at $r=r_{\mathrm{D}}^{\mathrm{c}}=10\sigma$ (unless otherwise stated). The NPs also experience torque induced by the dipole moments, see Eq. (2). The effect of this torque on the NP equations of motion is detailed in the SM.

The type of the third component, here NPs, determines ϕ_{33}^{tot} and the cross interaction potentials ϕ_{13} and ϕ_{23} between the third component and the polymer species P_1 and P_2, respectively. Models for effective interactions in various soft matter systems are covered by, e.g., Refs. 57,59,70–72. Here, colloidal NPs are dispersed in a two polymer component aqueous solution. Notably, species affinities in multicomponent solutions are generally asymmetric, meaning that the affinities of solute species in two polymer component solutions favor more interactions with one of the polymer components. In Ref. 19, the NPs mostly partition in the dextran rich phase. This is because dextran and the citrate-coated iron oxide NPs have favorable interactions [19].

For defining the cross interaction potentials ϕ_{13} and ϕ_{23}, we first consider prior literature. For a colloid-polymer mixture, a parameterized effective potential [73] has been reported. However, a common modeling approach for colloid-polymer mixtures is the so called Asakura–Oosawa–Vrij potential [74] used in, e.g., Refs. 75–77. In it, the interactions between the colloids and polymers are modeled via a hard-sphere potential. Here, a more realistic softer potential form, the purely repulsive WCA-potential, see Eq. (9), is used for interactions of P_1 and NPs. To simplify, $\sigma_{13}=\sigma$. This choice of potential models steric interactions, i.e., corresponds to a "neutral" affinity, which matches qualitatively the affinity response between PEG and NPs in Ref. 19. The actual interaction functional form between P_2 and the NP component is unknown, but attractive [19].

Due to the screened electrostatic interactions, the attractive interaction can be assumed to be short ranged, and to model this, we select the standard Mie potential [78]

$$\phi_{23}^{\mathrm{Mie}}(r)=4\varepsilon_{23}\left[\left(\frac{\sigma}{r}\right)^{48}-\left(\frac{\sigma}{r}\right)^{24}\right] \tag{11}$$

for the cross interaction of the higher NP affinity polymer species, P_2, and the NPs. Here, the diameter of P_2 is set to σ, and the geometrical

average of the species diameters is used to obtain the cross interaction range for NPs and P_2. The level of affinity is controlled by ϵ_{23}. In the simulations, ϕ_{23}^{Mie} is truncated at $r = 1.35\sigma$. The residual attraction value at this distance is smaller than 0.3% ϵ_{23}.

Potentials similar to Eq. (11) have been used to model, e.g. short-ranged interactions between colloids [79]. Other forms of short-ranged interaction potentials have been used to describe globular proteins [80], which are also modeled as hard colloids. One can thus expect that potential forms similar to Eq. (11) might be used to study the partitioning within ATPSs of a broad range of biomolecules.

Extracting systematic ϵ_{23} dependencies from experimental setups, such as the ATPS in Ref. 19, is arduous because the interaction functional form is unknown due to the complex partitioning mechanisms [7, 18,81,82]. We approach here matching the actual experimental systems by exploring different ϵ_{23} values vs NP partitioning response in a system where 5000 NPs ($\rho_{\text{NP}}\sigma^3 \approx 0.093$) with identical (reduced by $(4\pi k_{\text{B}}T\sigma^3\mu_0^{-1})^{1/2}$, where μ_0 is the vacuum permeability) dipole moment strength [83] $\mu_i = \mu = 2$ for all NPs $i = 1, ..., 5000$ are added to system A1 (see Table I). Assuming $\sigma = 10$ nm, the chosen dipole moment value $\mu = 2$ is approximately $4 \times 10^{-19}\text{Am}^2$. For comparison, *Sample 0* in Ref. 19 contains approximately 2250 NPs in the same volume (see SM). Here, the same $\sigma = 10$ nm value has been used in the estimate. This is equivalent to $\rho_{\text{NP}}^{\text{exp}}\sigma^3 \approx 0.042$. The estimated NP dipole moments of *Sample 0* are approximately $7 \times 10^{-20}\text{Am}^2$. In the latter, the average diameter of the magnetic core of the NPs was estimated to be 7 nm. We note that the choice of dipole moment strength for the NPs in the simulations is close to the higher bound of what is achievable experimentally for a magnetic NP with a diameter of 10 nm. As a consequence, the NPs in the simulations behave more like standard iron oxide particles with a diameter around 14-15 nm. Such NPs can form chains in an external magnetic field. Because the electrostatic repulsion of Eq. (8) makes the NPs in the simulations effectively larger (with a diameter of $\approx 1.3\sigma$, corresponding to 13 nm) and due to the simple re-scalability provided by Brownian dynamics simulation reduced units, we chose to keep the ratio between the sizes of the different species in the simulations unchanged.

The presence of the NPs changes the conditions for phase separation for two reasons. First, the NPs exclude volume available to the polymers. This alters the thermodynamic state point. Second, the attractive interaction of the NPs with P_2 via Eq. (11) locally enhances the aggregation of P_2. This means that the value of ϵ_{23} is important for the phase separation response. To map and demonstrate the effect of this choice, $\beta\epsilon_{23} = 1, 3$, and 4, corresponding to systems B1, B2, and B3, are examined. The system composition and parameter details are collected in Table I.

Figure 2 shows the assembly configurations and quantification of the assembly for different values of ϵ_{23}. The snapshots correspond to configurations after 50×10^6 time steps. The radial distribution function data are obtained by averaging over all particles and over the last 10% of the simulations. In system B1, the NPs remain relatively homogeneously distributed and are present in both phases. The radial distribution function corresponding to NP and the affinity polymer species P_2, g_{23}, shows a small peak at separations corresponding to close-distance correlation. However, no long-range correlation is observed. Long-range correlations are also absent in g_{33} for the system B1. On the other hand, system B2 presents a stronger phase separation between the two polymer phases, mediated by the attraction between NPs and P_2. The NPs partition dominantly into the P_2 rich phase, demonstrated by the clear long-range correlation in both g_{23} and g_{33}. In system B3, the partitioning of NPs into the P_2 phase becomes even more pronounced. The P_2 component drives the formation of P_2-NP clusters, where P_2 particles tend to "adsorb" multiple NPs on their surface. This behavior is reflected by the prominent first peak in g_{23}, shown in Fig. 2(e), as well as by the visual inspection of panel (c). This clustering results from the strong surface affinity between P_2 and NPs (via a high value of ϵ_{23}). These P_2-NP clusters are jammed, resulting in significantly hindered dynamics. This means that for modeling ATPSs response, the affinity set for system B3 is too high: an upper limit for the value of ϵ_{23} exists for the system to exhibit liquid-like behavior. For this reason, the setup corresponding to system B3 is not discussed any further. Basically, the performed mapping indicates a range over which asymmetric affinity in this type of three solute component system can vary so that the outcome varies from modestly preferential to highly selective partitioning, while still maintaining fluid-like character of the system.

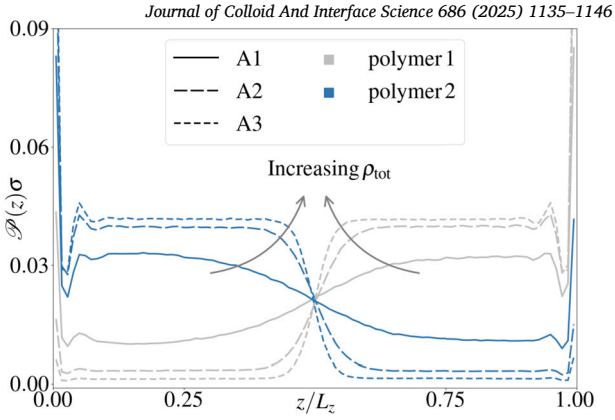

Fig. 3. Probability density $\mathscr{P}(z)$ of P_1 and P_2 in systems A1, A2, and A3. Gravity-like conditions are considered along the z axis, and the data is averaged over the production runs. Sketched arrows show the data trend with increasing total particle number density ρ_{tot} in the system.

Polymer-NP mixture under gravity-like conditions

The data of the previous section indicates that the phase separation is driven by polymer incompatibility, and the phase separation response is influenced by additional species via the affinities. A closer match with experimental systems in the modeling description requires considering also gravitational effects. Motivated by the reference ATPS [19], P_2 and the NPs are set to be heavier than P_1. Because of this, all P_2 and NPs are initially placed into the bottom half of the system and all P_1 initially occupy the region corresponding to the top half. Note that no explicit gravitational force is added to the model, but the system is allowed to evolve from this configuration. This is justified as the capillary length of the two-phase system in Ref. 19 is on the order of tens of μm but the linear dimension of the simulated system is on the order of μm. Equilibration is 150×10^6 time steps when NPs are present, and 300×10^6 time steps when the solution contains only polymers. After this, the production runs are 30×10^6 and 150×10^6 time steps, respectively, and presented data is calculated averaging over the production run.

Figure 3 presents the resulting z-axial probability density $\mathscr{P}$ for the different components in systems A1, A2, and A3, see Table I. $\mathscr{P}$ normalization is

$$\int_0^{L_z} \mathscr{P}(z)dz = 1. \tag{12}$$

The data shows that the degree of polymer P_1 and P_2 mixing decreases as the concentration of the polymers ρ_{tot} increases, as expected. Nevertheless, all examined systems exhibit a clear interface between the two phases at $z = L_z/2$. For system A1, the interface width is quite broad as the system is close to the critical concentration for phase separation. Unsurprisingly, $\mathscr{P}(z)$ is perfectly symmetric in terms of P_1 and P_2. The accumulation peaks at the walls are due to packing effects at the reflective (hard) wall.

Gravity-like conditions on polymer – polymer – nanoparticle systems was examined at the intermediate total polymer concentration, system A2. The effect of 5000 NPs was considered, and their affinity towards P_2 was varied as $\beta\epsilon_{23} = 1, 2$ and 3. The resulting systems are referred to as systems C1, C2, and C3, see Table I. Figure 4 shows the cross section visualizations of the systems at the end of the production runs, and the

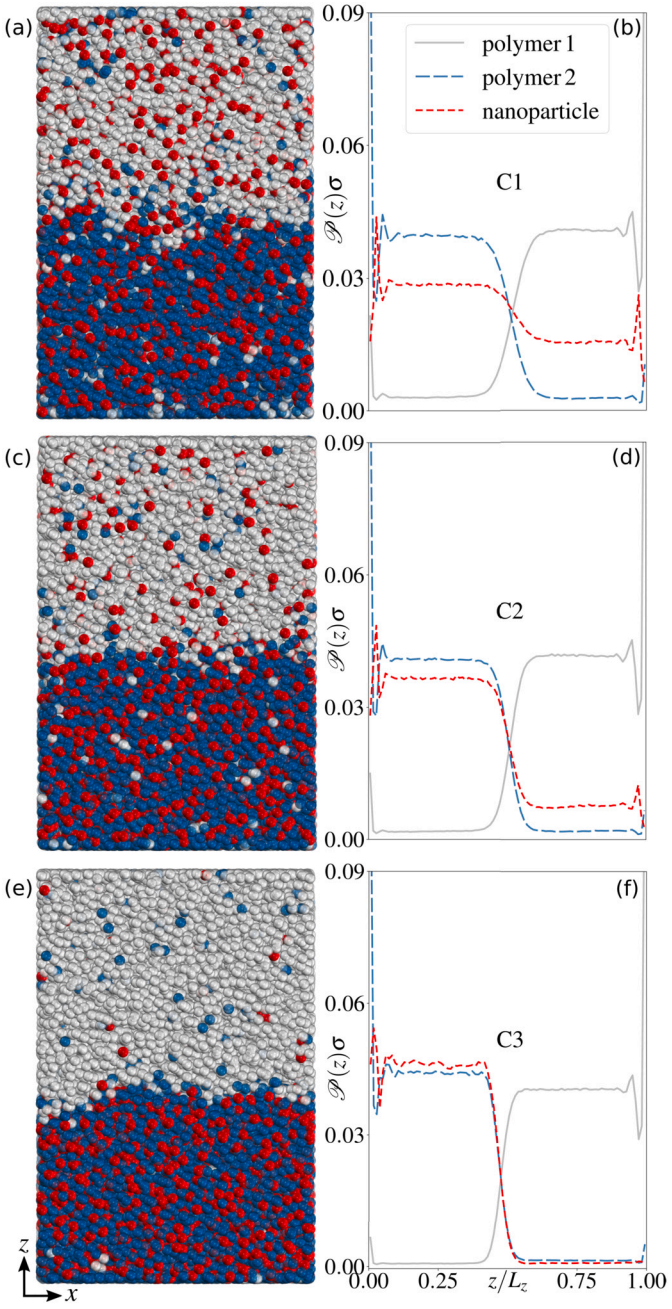

Fig. 4. Assembly configurations cross section visualizations (left column) and corresponding z-axial probability density of the different components (right column) for C1, C2, and C3 (top to bottom). P_1 are gray, P_2 blue, and NPs red.

corresponding probability density $\mathscr{P}(z)$. System C1, in which the NPs have low affinity to P_2, panels (a) and (b), has a practically identical polymer distribution as the system without NPs (system A2, Fig. 3). The NPs distribute slightly asymmetrically, due to small interaction preference with P_2.

Here, the z-axial distribution can be used to determine the phase boundary between the P_1 and P_2 rich phases. We consider the phase boundary to be the point where $\mathscr{P}(z)$ of P_1 and P_2 are equal. Let us call the fraction of NPs in the P_2 phase φ. For system C1, we find $\varphi \approx 63\%$, which means that the remaining 37% of NPs are in the P_1 phase. Increasing the affinity of NPs to P_2, in system C2 (see panels (c) and (d)) a more pronounced partitioning of the NPs with $\varphi \approx 81\%$ is found. The system with highest NP to P_2 affinity studied here, C3, (see panels (e) and (f)), results in an even stronger asymmetry of the distribution of the NPs with $\varphi \approx 96\%$, and only 4% of the NPs in the P_1 rich phase. Additionally, the interface moves towards the P_2 rich phase. This results in the coexisting density of P_2 increasing, i.e. both P_2 and NPs concentrations increase in the P_2 phase. In other words, system C3 demonstrates a case where the NPs enhance phase separation of the polymers, but also affect the packing density in their affinity phase. For completeness, Table II presents the calculated values of $\log_{10} P$, as is commonly measured in experiments. Here P is the ratio between the NPs densities in the two phases.

Table II
Dimensionless surface tensions γ^* and example values of the surface tension γ for $T = 298$ K and $\sigma = 10$ nm. φ is the fraction of NPs partitioned in the P_2 phase. Logarithm of the partition coefficient $\log_{10} P$ has been calculated in the simulation systems as the ratio of the plateau values of the NPs densities in the two phases. In our experiments, the value is obtained from Eq. (14). In Ref. 19, values of γ vary between 0.45 and 0.9 μN/m, and the ratio between the saturation magnetizations led to $\log_{10} P$ between 1.22 ± 0.09 and 1.07 ± 0.08, depending on the dilution of the sample.

System	γ^*	γ (μN/m)	φ	$\log_{10} P$
A1	0.004	0.16	-	-
A2	0.051	2.10	-	-
A3	0.125	5.14	-	-
C1	0.051	2.10	$63 \pm 1\%$	0.27 ± 0.01
C2	0.080	3.29	$81 \pm 1\%$	0.68 ± 0.01
C3	0.115	4.73	$96 \pm 1\%$	1.78 ± 0.02
E1	-	-	-	0.81 ± 0.01
E2	-	-	-	0.85 ± 0.01
E3	-	-	-	1.05 ± 0.01

The partitioning of the NPs in Ref. 19 is measured by estimating the NP concentration in each phase by probing the local density, light absorption, and the magnetic properties. Interestingly, the measured partitioning varies depending on the level of dilution of the samples between 91% and 94% of the NPs in their affinity phase, i.e., the dextran rich phase. In a system close to the phase separation critical point, the small changes in partitioning are a signal of a strong preference of the NPs to be close to the dextran molecules in the experimental setup of Ref. 19.

Our findings indicate that at least two handles for controlling the partitioning of a third component in an ATPS exist. First, the thermodynamic state point provides a direct handle by controlling the coexisting densities of the polymer mixture. Second, a handle is obtained by tuning the coupling between the density distribution of the polymers and the partitioned component, in the model via $\beta\epsilon_{23}$, and in the experiments through the affinity between the partitioning component and the two polymers. Our model provides direct access to partitioning response by both means of control, and has thus the potential to provide prediction trends for partitioning in an easily verifiable way. This is demonstrated by the experimental results, see next section.

An important connection point with actual ATPSs is the (reduced) surface tension γ^* [8] between the P_1 and P_2 rich phases:

$$\gamma^* = -\int_{z_1}^{z_2} \left[\langle \varsigma_{zz}(z) \rangle - \frac{\langle \varsigma_{xx}(z) \rangle + \langle \varsigma_{yy}(z) \rangle}{2} \right] dz. \tag{13}$$

Here ς_{ii} for $i = x, y, z$ are the diagonal components of the stress tensor. For calculating γ^*, we set $z_1 = L_z/4$ and $z_2 = 3L_z/4$ for all other systems except A1, where $z_1 = L_z/6$ and $z_2 = 5L_z/6$ due to the broad interface. The resulting surface tension estimates for all considered systems are summarized for comparison in Table II. In this, the estimate for surface tension $\gamma = \gamma^* k_B T \sigma^{-2}$ is calculated for $T = 298$ K and $\sigma = 10$ nm.

While surface tension dependency on polymer species and phase separation are well-known, it is enlightening to examine the model performance in terms of this. The data shows that the addition of NPs with

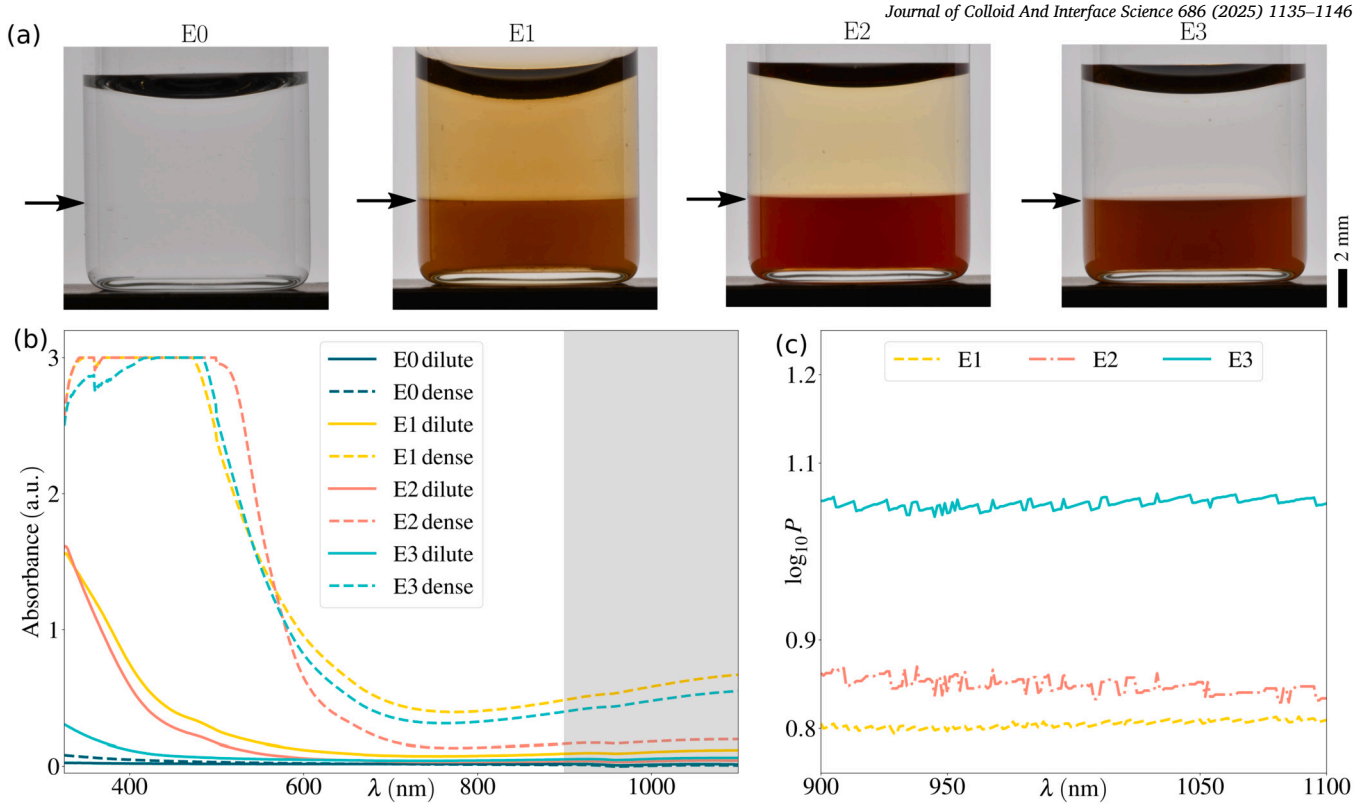

Fig. 5. (a) Photographs of the vials used for the spectrophotometry experiments for systems E0, E1, E2, and E3. The arrows indicate the position of the interface in each system. (b) Raw data profiles of the light absorption as a function of the wavelength λ for both dense and dilute phases of each sample. (c) Calculated $\log_{10} P$ value for the dispersions of NPs in ATPSs E1, E2, and E3 as a function of λ in the range corresponding to the shaded region in panel (b).

relatively low affinity to P_2 ($\beta\varepsilon_{23} = 1$) does not have a significant effect on the surface tension. On the other hand, increasing the affinity leads to the surface tension increasing by up to a factor of ≈ 2.3 for $\beta\varepsilon_{23} = 3$. These values are well in the range of surface tensions commonly measured experimentally for ATPSs [19,84]. The surface tension is also expected to depend on the NP concentration, however, this is not explored in this work. Also, since $\gamma = \gamma^* k_B T \sigma^{-2}$, and the value of σ in real units is not fixed in the modeling, the size of the polymers provides an evident control means for the surface tension. In colloid-polymer binary mixtures, the colloidal diameter provides similar handle [85]. Additionally, the surface tension also depends on the difference between the coexisting densities in the two phases, vanishing at the critical point [64].

Even though the presented polymer – polymer – NP modeling approach was developed for capturing partitioning trends in generic ATPSs, the range of surface tension values obtained using $\sigma = 10$ nm is rather satisfactory. The employed σ value is realistic based on Ref. 19. However, the simplification $R_{11} = R_{22} = R$ does not correspond to the size ratio of dextran and PEG in Ref. 19. The phase diagram is known to change based on R_{ij} [64], which means that the phase diagram variation cannot be generalized as a function of R_{ij}. Furthermore, more precise predictions of both partitioning and surface tension could be obtained by fitting the thermodynamic state point of the model to match the coexisting phase densities of the experimental system.

Note that we investigated the effect of the dipole-dipole cutoff distance r_D^c on both partitioning and surface tension, and found very marginal changes in the predictions.

3.2. ATPS partitioning results in experiments

Analogous variation of NP affinity to the polymers as in the simulation results of Fig. 4 was obtained in an experimental setup by varying the coating of iron oxide NPs in a PEG-dextran ATPS. The NP-free PEG-dextran ATPS is referred to as system E0. The following NPs were selected: PBG300 pegylated iron oxide NPs from Ferrotec (E1), synthesized dispersion of citrate-coated iron oxide NPs [19] (E2), and 45-111-701 phospholipid coated iron oxide NPs from Micromod (E3). As the affinities of the NPs with PEG and dextran differ, the partitioning in systems E1, E2, and E3 is visibly different (Fig. 5(a)). The driving mechanism that leads to the differences in partitioning of NPs in ATPS systems is complex and difficult to rationalize [7,18]. For example, citrate-coated gold NPs are known to partition to the PEG phase [81,82], oppositely to what we have demonstrated for the case of citrate-coated iron oxide NPs. In this work, the choice of different coatings is presented as proof of the concept that the affinity can be regulated to achieve distinct levels of partitioning for iron oxide NPs in an ATPS. A quantitative estimation of the partitioning was obtained by the light absorption of the dilute and dense phases (in terms of NPs concentration) of each sample, measured using a spectrophotometer (Fig. 5(b)). After subtracting the signal contribution rising from the polymers, the partitioning coefficient P, commonly used to characterize partitioning within ATPSs [18], was evaluated using the Beer-Lambert law for light absorption:

$$\log_{10} P = \log_{10}\left(A_{\text{dense}}/A_{\text{dilute}}\right), \tag{14}$$

where A_{dense} and A_{dilute} are the (wavelength dependent) absorption of the dense and the dilute phase, respectively (see Ref. 19, Supplementary note 6)). The logarithmic form connects directly to the energetics of the system, such as chemical potential, enthalpy, entropy, and Gibbs free energy [86]. The calculated values of $\log_{10} P$ at different wavelengths λ (Fig. 5(c)) were averaged to obtain 0.81 ± 0.01 for E1, 0.85 ± 0.01 for E2, and 1.05 ± 0.01 for E3 (see Table II).

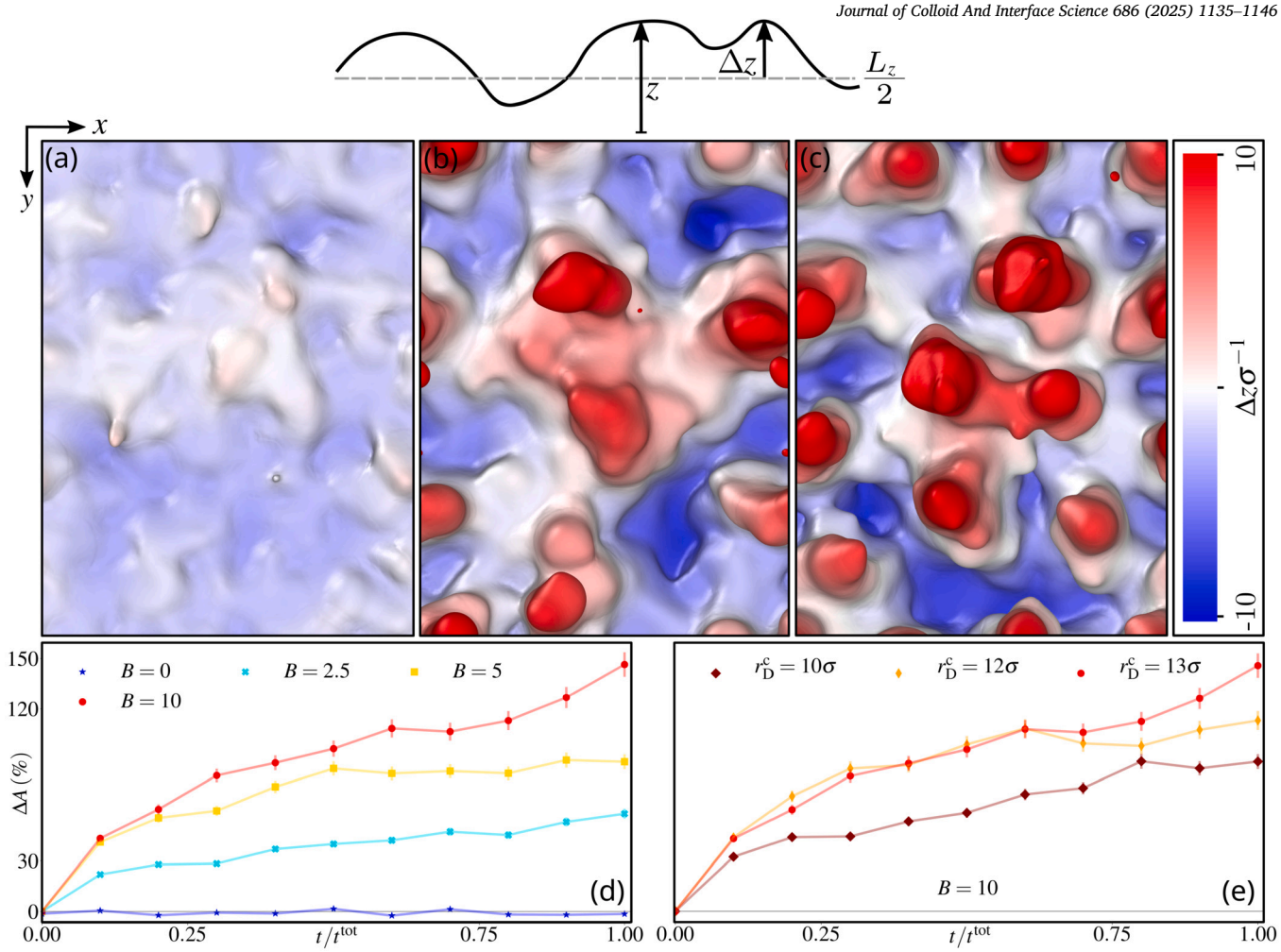

Fig. 6. Height changes of the bottom phase for C3 after 25×10^6 steps with magnetic dipole - dipole interaction cut-off $r_D^c = 13\sigma$ (a) before turning on B, (b) after 50×10^6 time steps with $B = 5$, and (c) with $B = 10$. (d) Relative surface area change ΔA over time, for different values of B. (e) The effect of magnetic dipole - dipole interaction cut-off r_D^c on ΔA for $B = 10$. The simulation time t and total simulation time $t^{tot} = 50 \times 10^6$ are measured in simulation time steps.

3.3. Effect of external magnetic field on NP–ATPS in the computational model

Let us next consider the effect of an external magnetic field on the polymer mixture and NPs model under gravity-like conditions. The equilibrated system C3, Fig. 4(e), is considered as it best matches the experimental reference setup [19]. An external magnetic field $\mathbf{B} = B\mathbf{e}_z$, where B is the reduced magnetic field strength [83] and $\mathbf{e}_z$ is a z-axial unit vector, is applied on the system. The system is first equilibrated for 25×10^6 steps with magnetic dipole-dipole interaction cut-off $r_D^c = 13\sigma$. In addition to the dipole-dipole interactions (force and torque), the external magnetic field imposes a further torque $\mathbf{T}^B = \boldsymbol{\mu} \times \mathbf{B}$ on the magnetic NPs. The charges of the NPs are considered via Eq. (8) as effective contributions. This approximation allows excluding the interaction contributions due to magnetic field-charge interactions. For strong enough magnetic field, the dipole moments align in the direction of $\mathbf{B}$ (here the z axis). This gives rise to long range dipole-dipole correlations. One can expect that the interface experiences modulation, potentially resulting in a variety of patterns.

Let us next consider the expected characteristic lengths involved in these patterns to assess appropriate models and interpretations of systems responses. For a dilute ferrofluid and small magnetic field, the relative permeability of the magnetic (bottom) phase is $\mu_r = 1 + \mu_0 \rho_B \mu^2 (k_B T)^{-1}$. In this, μ_0 is the permeability of vacuum and ρ_B is the number density of NPs in the ferrofluid phase [36]. In system C3, $\rho_B \approx 5000 \times 0.96 \,/\, (30 \times 40 \times 22.5\,\sigma^3) \approx 0.18\,\sigma^{-3}$. This corresponds to relative permeability $\mu_r \approx 10$. The classic Rosensweig instability of sharp-interface ferrofluids [36] results in patterns with a characteristic length larger than

$$\lambda^* = 2\pi \frac{\gamma \mu_0 \mu_r (1 + \mu_r)}{(\mu_r - 1)^2 B^2}, \tag{15}$$

calculated by setting the dispersion relation

$$\omega(q) = \left[g\Delta\rho - \frac{(\mu_r - 1)^2}{\Delta\rho \mu_0 \mu_r (1 + \mu_r)} B^2 q^2 + \frac{\gamma}{\Delta\rho} q^3 \right]^{1/2} \tag{16}$$

to zero in the absence of gravity, i.e. $g = 0$, and solve for the critical wave number $q^* = 2\pi/\lambda^*$. Note that $\Delta\rho$ is the number density difference between the two phases. The value of λ^* is dependent on B, and hence, a value for B needs to be chosen to extract expected patterns scales. The surface tension $\gamma = 4.73$ μN/m of system C3 and choosing a representative magnetic field strength of $B = 1$ (in real units approximately 16 mT [83]; In Ref. 19, typical comparison values are on the order of 10 mT) results in a lower limit $\lambda^* \approx 4\pi\sigma$. Since this is on the order of the size of the particles, continuum theory cannot be expected to work quantitatively in this regime, and particle-based simulations are a more appropriate approach to resolve the interface response here. In our experiments [19], the periodicity of the patterns rising at the interface of this particular ATPS system was observed to be on the order of 100 – 300 μm. To the best of our knowledge, these pattern periodicities are the shortest so far measured for Rosensweig-type instability at the

interface between continuous phases. The current modeling approach allows, however, to reach periodicity scales so small as approximately $5-10\sigma$ (between tens of nm and μm, depending on the size of the solutes). The emergence of the patterning also at these smaller lengths scales in the simulations could promote pursuing the feature in actual ferrofluids as well.

Figure 6 shows the response of the modeled system to external magnetic field via Δz, the interface height deviation from $L_z/2$. The sketch at the top presents the variables. The iso-surface map parameters used for the visualization are a radius scaling of 2×, iso-value 3, and the radii of both NPs and P_2 are set to $\sigma/2$. Before the magnetic field is turned on, the interface is relatively flat with oscillations that are on the order of one or two particle diameters, see panel (a). These fluctuations are due to the liquid nature of the system (capillary waves). We then set B =2.5, 5 and 10, and run the simulations for 50×10^6 time steps, corresponding to t^{tot} in Fig. 6(d). For $B=5$, clearly enhanced fluctuations of the interface are present, see Fig. 6(b). A stronger magnetic field, $B=10$, increases these oscillations, see panel (c). Panel (d) quantifies the effect of the magnetic field on the interface by the relative surface area change ΔA over time. The change is measured with respect to the initial surface area. The data shows that this change increases over time. The area change measured at t^{tot} depends monotonically on the strength of B. The corresponding change of surface area for $B=0$, which is smaller than ±5%, is shown for comparison. Notably, the modeling outcome is dependent on the magnetic dipole - dipole interaction cut-off $r_{\mathrm{D}}^{\mathrm{c}}$ and in panel (e) this dependency is explored: the magnetic field driven modulation of the interface increases with $r_{\mathrm{D}}^{\mathrm{c}}$. For numerical reasons, the model requires a cut-off and this dependency presents multiple challenges: here we note the existence and influence of the effect. Despite this approximation, we note that the model captures the expected trend, and we find a convergence of the prediction as the cut-off length is increased.

The interface modulation predicted by our computational model is more dynamic than the one observed in the experimental reference system of Ref. 19. Additionally, the modulation in the simulations does not exhibit a periodic structure, opposed to the stationary patterns of Ref. 19. Close scrutiny of the interface modulation reveals the formation of zippered chains that disrupt the polymer-polymer interface. These columns vary in size (both in height and in width), and include single NP-chains as well as broad multi-chain assemblies. Due to system size constraints, it is difficult to conclude if this modulation is a precursor of a typical Rosensweig instability, such as those reported in Ref. 19, or if the interaction between the interface and the magnetic field drives the formation of zippered chains (see Fig. 1 of the SM). Nevertheless, the modeling shows that such coarse-grained models as the one developed here can extract magnetic self-organization and interface instability responses.

4. Conclusions

We presented a general coarse-grained Brownian dynamics-based simulation approach to study phase separation of aqueous polymer mixtures and the partitioning of an arbitrary third component in the mixture. Motivated by the experiments of Ref. 19, the model was employed to investigate the segregation of magnetic NPs and their response to an external magnetic field. The key feature of our approach relies on the effective interaction between the immiscible polymers. Here, these polymers were described by a so-called Gaussian core model, which is particularly accurate for interactions of linear polymers in good solvents [55] and also captures phase separation behavior [62].

The computational model is demonstrated against the model ATPS of Ref. 19. The modeling findings demonstrate that at least two handles for controlling the partitioning of a third component in a polymer-based ATPS exist. The first handle is via the thermodynamic state point, which controls the coexisting densities of the polymer mixture. The second handle is the affinity and its asymmetry between the partitioned component and the polymer species. As partitioning in ATPSs is key to most of their applications [12,18,87], we compared the model predictions against experiments. Even though the computational model was not explicitly parametrized to match the reference system [19], predictions of the NPs partitioning were well within the range of experimentally measured values for different NP species. Important for designing ATPSs with desired partitioning response, the work revealed the sensitivity of the system partitioning response to interactions parameters (the component affinities). In our experiments, we achieved such control by varying the surface coating of the NPs to tune the affinity to polymer species. Side-by-side, the modeling predicted trends and the experimentally achieved tuning of the NP affinity demonstrate a practical design handle.

Our results also show that thermodynamic quantities, such as the interfacial tension, can be obtained using the presented modeling approach. Small interfacial tensions, common in many biomolecular systems, and more generally in ATPSs, are often challenging to capture experimentally - our computational approach can be used to calculate such quantities, which then can be connected to analytical expressions to forecast trends. Overall, the values of the surface tension estimated from our computational model for the different ATPSs were demonstrated to be well within experimentally measured ranges [19,84], see also Table II and its caption. The comparison of the different ATPSs in the computational modeling also revealed an often overlooked dependency of the surface tension between the phases on the affinity between the third component and the polymer species.

Finally, our particle-based approach readily allows studying the response of magnetic particles also under external magnetic field in ATPSs. As previously measured experimentally for the reference system [19], also our computational model exhibits interface modulations under external magnetic fields. However, the interface fluctuations observed in the simulations occurred on much smaller length scales, exhibited less periodic structures, and were more dynamic than those in experiments. The surface modulation is characterized by the formation of zippered chains of NPs, as can be seen in Fig. 1 of the SM. This could be either a precursor to the standard Rosensweig instability or arise from a competition between the surface tension and the formation of zippered chains, which simultaneously draw the polymers to increase the surface area of the interface. Our findings demonstrate that the coarse-grained simulation approach has the potential to resolve coupled magnetic self-organization and interfacial instabilities in ATPSs. In closing, our approach to modeling ATPSs with or without a third solute species is readily generalizable to examining the influence of solute species affinities and system compositions on partitioning and the phase separation response of general two-phase solutions. This leads us to anticipate exciting applications in considering biomolecular extraction, purification and separation approaches, more generally colloidal self-organization, and also extracting guidelines for driving assembly in complex multicomponent solutions that exhibit phase separation – here demonstrated by magnetic nanoparticles and external magnetic field.

CRediT authorship contribution statement

Alberto Scacchi: Writing – original draft, Visualization, Validation, Software, Resources, Methodology, Investigation, Funding acquisition, Formal analysis, Data curation, Conceptualization. **Carlo Rigoni:** Writing – original draft, Visualization, Investigation, Formal analysis, Data curation. **Mikko Haataja:** Writing – review & editing, Methodology, Funding acquisition, Conceptualization. **Jaakko V.I. Timonen:** Writing – review & editing, Supervision, Resources, Funding acquisition, Conceptualization. **Maria Sammalkorpi:** Writing – review & editing, Supervision, Resources, Funding acquisition, Conceptualization.

Declaration of competing interest

The authors declare that they have no known competing financial interests or personal relationships that could have appeared to influence the work reported in this paper.

Acknowledgements

This work was supported by the Swiss National Science Foundation under the project no. P500PT_206916 (A.S.) and the Academy of Finland through its Centres of Excellence Programs (2022-2029, LIBER) under projects no. 346111 and 364205 (M.S.) and 346112 and 364206 (J.T.). MPH was supported by the National Science Foundation through the Princeton University (PCCM) Materials Research Science and Engineering Center DMR-2011750. A.S. warmly thanks Bob Evans for extensive scientific discussions and for his hospitality during the research visit in Bristol. Computational resources by CSC IT Centre for Finland, the Aalto Science-IT project, and RAMI – RawMatters Finland Infrastructure are also gratefully acknowledged.

Appendix A. Supplementary material

Supplementary material related to this article can be found online at https://doi.org/10.1016/j.jcis.2025.01.256.

Data availability

Link to the inputs of the simulations and data is provided at https://doi.org/10.23729/4fb80194-cdb2-4f49-94f4-f8a87b8e29c1. If using the inputs or the open data, we request acknowledging the authors by citing the original source.

References

[1] C.P. Brangwynne, P. Tompa, R.V. Pappu, Polymer physics of intracellular phase transitions, Nat. Phys. 11 (11) (2015) 899–904.
[2] A.A. Hyman, C.A. Weber, F. Jülicher, Liquid–liquid phase separation in biology, Annu. Rev. Cell Dev. Biol. 30 (2014) 39–58.
[3] S. Alberti, D. Dormann, Liquid–liquid phase separation in disease, Annu. Rev. Genet. 53 (2019) 171–194.
[4] S. Alberti, A. Gladfelter, T. Mittag, Considerations and challenges in studying liquid-liquid phase separation and biomolecular condensates, Cell 176 (3) (2019) 419–434.
[5] F. Wang, P. Altschuh, L. Ratke, H. Zhang, M. Selzer, B. Nestler, Progress report on phase separation in polymer solutions, Adv. Mater. 31 (26) (2019) 1806733.
[6] S. Raja, V.R. Murty, V. Thivaharan, V. Rajasekar, V. Ramesh, Aqueous two phase systems for the recovery of biomolecules–a review, Sci. Technol. 1 (1) (2011) 7–16.
[7] J.A. Asenjo, B.A. Andrews, Aqueous two-phase systems for protein separation: a perspective, J. Chromatogr. A 1218 (49) (2011) 8826–8835.
[8] E. Atefi, R. Joshi, J.A. Mann Jr., H. Tavana, Interfacial tension effect on cell partition in aqueous two-phase systems, ACS Appl. Mater. Interfaces 7 (38) (2015) 21305–21314.
[9] R.C. Assis, A.B. Mageste, L.R. de Lemos, R.M. Orlando, G.D. Rodrigues, Application of aqueous two-phase system for selective extraction and clean-up of emerging contaminants from aqueous matrices, Talanta 223 (2021) 121697.
[10] Y. Chao, H.C. Shum, Emerging aqueous two-phase systems: from fundamentals of interfaces to biomedical applications, Chem. Soc. Rev. 49 (1) (2020) 114–142.
[11] P. Rosa, I. Ferreira, A. Azevedo, M. Aires-Barros, Aqueous two-phase systems: a viable platform in the manufacturing of biopharmaceuticals, J. Chromatogr. A 1217 (16) (2010) 2296–2305.
[12] H. Walter (Ed.), Partitioning in Aqueous Two–Phase System: Theory, Methods, Uses, and Applications to Biotechnology, 1st edition, Academic Press, Oxford, UK, 1985.
[13] A.G. Teixeira, R. Agarwal, K.R. Ko, J. Grant-Burt, B.M. Leung, J.P. Frampton, Emerging biotechnology applications of aqueous two-phase systems, Adv. Healthc. Mater. 7 (6) (2018) 1701036.
[14] J.F. Pereira, M.G. Freire, J.A. Coutinho, Aqueous two-phase systems: towards novel and more disruptive applications, Fluid Phase Equilib. 505 (2020) 112341.
[15] A. Zbinden, M. Pérez-Berlanga, P. De Rossi, M. Polymenidou, Phase separation and neurodegenerative diseases: a disturbance in the force, Dev. Cell 55 (1) (2020) 45–68.
[16] S. Jiang, J.B. Fagman, C. Chen, S. Alberti, B. Liu, Protein phase separation and its role in tumorigenesis, eLife 9 (2020) e60264.
[17] R. Hatti-Kaul, Aqueous two-phase systems, Mol. Biotechnol. 19 (3) (2001) 269–277.
[18] M. Iqbal, Y. Tao, S. Xie, Y. Zhu, D. Chen, X. Wang, L. Huang, D. Peng, A. Sattar, M.A.B. Shabbir, H.I. Hussain, S. Ahmed, Z. Yuan, Aqueous two-phase system (ATPS): an overview and advances in its applications, Biol. Proced. Online 18 (1) (2016) 1–18.
[19] C. Rigoni, G. Beaune, B. Harnist, F. Sohrabi, J.V.I. Timonen, Ferrofluidic aqueous two-phase system with ultralow interfacial tension and micro-pattern formation, Commun. Mater. 3 (26) (2022) 1–11.
[20] X. Zhang, L. Sun, Y. Yu, Y. Zhao, Flexible ferrofluids: design and applications, Adv. Mater. 31 (51) (2019) 1903497.
[21] M. Maiorov, A. Cebers, Magnetic microconvection on the diffusion front of ferroparticles, Magnetohydrodynamics 19 (4) (1983) 376–380.
[22] I. Torres-Díaz, C. Rinaldi, Recent progress in ferrofluids research: novel applications of magnetically controllable and tunable fluids, Soft Matter 10 (43) (2014) 8584–8602.
[23] S.Y. Lee, J. Choi, J.-R. Jeong, J.H. Shin, S.-H. Kim, Magnetoresponsive photonic microspheres with structural color gradient, Adv. Mater. 29 (13) (2017) 1605450.
[24] M. Zou, J. Wang, Y. Yu, L. Sun, H. Wang, H. Xu, Y. Zhao, Composite multifunctional micromotors from droplet microfluidics, ACS Appl. Mater. Interfaces 10 (40) (2018) 34618–34624.
[25] T. Cherian, F. Sohrabi, C. Rigoni, O. Ikkala, J.V.I. Timonen, Electroferrofluids with nonequilibrium voltage-controlled magnetism, diffuse interfaces, and patterns, Sci. Adv. 7 (52) (2021) eabi8990.
[26] M. Kole, S. Khandekar, Engineering applications of ferrofluids: a review, J. Magn. Magn. Mater. 537 (2021) 168222.
[27] H. Xia, J. Wang, Y. Tian, Q.-D. Chen, X.-B. Du, Y.-L. Zhang, Y. He, H.-B. Sun, Ferrofluids for fabrication of remotely controllable micro-nanomachines by two-photon polymerization, Adv. Mater. 22 (29) (2010) 3204–3207.
[28] K. Ulbrich, K. Hola, V. Subr, A. Bakandritsos, J. Tucek, R. Zboril, Targeted drug delivery with polymers and magnetic nanoparticles: covalent and noncovalent approaches, release control, and clinical studies, Chem. Rev. 116 (9) (2016) 5338–5431.
[29] K. Hayashi, W. Sakamoto, T. Yogo, Smart ferrofluid with quick gel transformation in tumors for mri-guided local magnetic thermochemotherapy, Adv. Funct. Mater. 26 (11) (2016) 1708–1718.
[30] A. Afifah, S. Syahrullail, N. Sidik, Magnetoviscous effect and thermomagnetic convection of magnetic fluid: a review, Renew. Sustain. Energy Rev. 55 (2016) 1030–1040.
[31] C.-Y. Chen, Z.-Y. Cheng, An experimental study on Rosensweig instability of a ferrofluid droplet, Phys. Fluids 20 (5) (2008) 054105.
[32] R.E. Rosensweig, M. Zahn, R. Shumovich, Labyrinthine instability in magnetic and dielectric fluids, J. Magn. Magn. Mater. 39 (1–2) (1983) 127–132.
[33] M. Igonin, A. Cebers, Labyrinthine instability of miscible magnetic fluids, Phys. Fluids 15 (6) (2003) 1734–1744.
[34] S. Echeverría-Alar, M. Clerc, Labyrinthine patterns transitions, Phys. Rev. Res. 2 (4) (2020) 042036.
[35] H. Kadau, M. Schmitt, M. Wenzel, C. Wink, T. Maier, I. Ferrier-Barbut, T. Pfau, Observing the Rosensweig instability of a quantum ferrofluid, Nature 530 (7589) (2016) 194–197.
[36] R.E. Rosensweig, Ferrohydrodynamics, Courier Corporation, Mineola, New York, 2013.
[37] P. Espanol, P.B. Warren, Perspective: dissipative particle dynamics, J. Chem. Phys. 146 (15) (2017) 150901.
[38] G.A. Huber, J.A. McCammon, Brownian dynamics simulations of biological molecules, Trends Geochem. 1 (8) (2019) 727–738.
[39] A. Muñiz-Chicharro, L.W. Votapka, R.E. Amaro, R.C. Wade, Brownian dynamics simulations of biomolecular diffusional association processes, WIREs Comput. Mol. Sci. 13 (3) (2023) e1649.
[40] M. Müller, J.J. de Pablo, Computational approaches for the dynamics of structure formation in self-assembling polymeric materials, Annu. Rev. Mater. Res. 43 (1) (2013) 1–34.
[41] M. Müller, Process-directed self-assembly of copolymers: results of and challenges for simulation studies, Prog. Polym. Sci. 101 (2020) 101198.
[42] J.F. Lutsko, Recent developments in classical density functional theory, Adv. Chem. Phys. 144 (2010) 1.
[43] M. te Vrugt, H. Löwen, R. Wittkowski, Classical dynamical density functional theory: from fundamentals to applications, Adv. Phys. 69 (2) (2020) 121–247.
[44] M. Schmidt, Power functional theory for many-body dynamics, Rev. Mod. Phys. 94 (1) (2022) 015007.
[45] A. Argun, A. Callegari, G. Volpe, Brownian dynamics, in: Simulation of Complex Systems, 2053-2563, IOP Publishing, 2021, pp. 5-1–5-13.
[46] I.M. Ilie, W.J. Briels, W.K. den Otter, An elementary singularity-free rotational Brownian dynamics algorithm for anisotropic particles, J. Chem. Phys. 142 (11) (2015) 114103.
[47] P. Langevin, Sur la théorie du mouvement brownien, C. R. Acad. Sci. 146 (1908) 530–532.
[48] A.P. Thompson, H.M. Aktulga, R. Berger, D.S. Bolintineanu, W.M. Brown, P.S. Crozier, P.J. in 't Veld, A. Kohlmeyer, S.G. Moore, T.D. Nguyen, R. Shan, M.J. Stevens, J. Tranchida, C. Trott, S.J. Plimpton, LAMMPS - a flexible simulation tool for particle-based materials modeling at the atomic, meso, and continuum scales, Comput. Phys. Commun. 271 (2022) 108171.

[49] P.J. in't Veld, S.J. Plimpton, G.S. Grest, Accurate and efficient methods for modeling colloidal mixtures in an explicit solvent using molecular dynamics, Comput. Phys. Commun. 179 (5) (2008) 320–329.
[50] T. Shire, K.J. Hanley, K. Stratford, DEM simulations of polydisperse media: efficient contact detection applied to investigate the quasi-static limit, Comput. Part. Mech. 8 (4) (2021) 653–663.
[51] L. Martínez, R. Andrade, E.G. Birgin, J.M. Martínez, PACKMOL: a package for building initial configurations for molecular dynamics simulations, J. Comput. Chem. 30 (13) (2009) 2157–2164.
[52] A.I. Jewett, D. Stelter, J. Lambert, S.M. Saladi, O.M. Roscioni, M. Ricci, L. Autin, M. Maritan, S.M. Bashusqeh, T. Keyes, R.T. Dame, J.-E. Shea, G.J. Jensen, D.S. Goodsell, Moltemplate: a tool for coarse-grained modeling of complex biological matter and soft condensed matter physics, J. Mol. Biol. 433 (11) (2021) 166841.
[53] W. Humphrey, A. Dalke, K. Schulten, VMD: visual molecular dynamics, J. Mol. Graph. Model. 14 (1) (1996) 33–38.
[54] A. Stukowski, Visualization and analysis of atomistic simulation data with OVITO–the open visualization tool, Model. Simul. Mater. Sci. Eng. 18 (1) (2009) 015012.
[55] A. Louis, P. Bolhuis, J. Hansen, E. Meijer, Can polymer coils be modeled as "soft colloids"?, Phys. Rev. Lett. 85 (12) (2000) 2522.
[56] P. Bolhuis, A. Louis, J. Hansen, E. Meijer, Accurate effective pair potentials for polymer solutions, J. Chem. Phys. 114 (9) (2001) 4296–4311.
[57] C.N. Likos, Effective interactions in soft condensed matter physics, Phys. Rep. 348 (4) (2001) 267–439.
[58] I. Götze, H. Harreis, C. Likos, Tunable effective interactions between dendritic macromolecules, J. Chem. Phys. 120 (16) (2004) 7761–7771.
[59] C.N. Likos, Soft matter with soft particles, Soft Matter 2 (6) (2006) 478–498.
[60] I. Götze, A.J. Archer, C. Likos, Structure, phase behavior, and inhomogeneous fluid properties of binary dendrimer mixtures, J. Chem. Phys. 124 (8) (2006) 084901.
[61] E. Antoniou, M. Tsianou, Solution properties of dextran in water and in formamide, J. Appl. Polym. Sci. 125 (3) (2012) 1681–1692.
[62] A. Louis, P. Bolhuis, J. Hansen, Mean-field fluid behavior of the Gaussian core model, Phys. Rev. E 62 (6) (2000) 7961.
[63] P.J. Flory, Principles of Polymer Chemistry, Cornell University Press, Ithaca, NY, US, 1953.
[64] A. Archer, R. Evans, Binary Gaussian core model: fluid-fluid phase separation and interfacial properties, Phys. Rev. E 64 (4) (2001) 041501.
[65] J.-P. Hansen, I.R. McDonald, Theory of Simple Liquids: with Applications to Soft Matter, 4th edition, Academic Press, Oxford, UK, 2013.
[66] Y. Na, S. Yang, S. Lee, Evaluation of citrate-coated magnetic nanoparticles as draw solute for forward osmosis, Desalination 347 (2014) 34–42.
[67] S. Safran, Statistical Thermodynamics of Surfaces, Interfaces, and Membranes, 1st edition, CRC Press, Boca Raton, FL, US, 2003.
[68] J.D. Weeks, D. Chandler, H.C. Andersen, Role of repulsive forces in determining the equilibrium structure of simple liquids, J. Chem. Phys. 54 (12) (1971) 5237–5247.
[69] D.J. Tildesley, M.P. Allen, Computer Simulation of Liquids, Oxford University Press, Oxford, UK, 1987.
[70] L. Belloni, Colloidal interactions, J. Phys. Condens. Matter 12 (46) (2000) R549.
[71] A. Narros, A.J. Moreno, C.N. Likos, Influence of topology on effective potentials: coarse-graining ring polymers, Soft Matter 6 (11) (2010) 2435–2441.
[72] J.J. McManus, P. Charbonneau, E. Zaccarelli, N. Asherie, The physics of protein self-assembly, Curr. Opin. Colloid Interface Sci. 22 (2016) 73–79.
[73] P. Bolhuis, A. Louis, How to derive and parameterize effective potentials in colloid-polymer mixtures, Macromolecules 35 (5) (2002) 1860–1869.
[74] S. Asakura, F. Oosawa, On interaction between two bodies immersed in a solution of macromolecules, J. Chem. Phys. 22 (7) (1954) 1255–1256.
[75] M. Dijkstra, J.M. Brader, R. Evans, Phase behaviour and structure of model colloid-polymer mixtures, J. Phys. Condens. Matter 11 (50) (1999) 10079.
[76] K. Binder, P. Virnau, A. Statt, Perspective: the Asakura Oosawa model: a colloid prototype for bulk and interfacial phase behavior, J. Chem. Phys. 141 (14) (2014) 559.
[77] D. Stopper, R. Roth, H. Hansen-Goos, Structural relaxation and diffusion in a model colloid-polymer mixture: dynamical density functional theory and simulation, J. Phys. Condens. Matter 28 (45) (2016) 455101.
[78] G. Mie, Zur kinetischen theorie der einatomigen Körper, Ann. Phys. 316 (8) (1903) 657–697.
[79] J. Rouwhorst, C. Ness, S. Stoyanov, A. Zaccone, P. Schall, Nonequilibrium continuous phase transition in colloidal gelation with short-range attraction, Nat. Commun. 11 (1) (2020) 3558.
[80] G. Foffi, G.D. McCullagh, A. Lawlor, E. Zaccarelli, K.A. Dawson, F. Sciortino, P. Tartaglia, D. Pini, G. Stell, Phase equilibria and glass transition in colloidal systems with short-ranged attractive interactions: application to protein crystallization, Phys. Rev. E 65 (3) (2002) 031407.
[81] M.R. Helfrich, M. El-Kouedi, M.R. Etherton, C.D. Keating, Partitioning and assembly of metal particles and their bioconjugates in aqueous two-phase systems, Langmuir 21 (18) (2005) 8478–8486.
[82] M.S. Long, C.D. Keating, Nanoparticle conjugation increases protein partitioning in aqueous two-phase systems, Anal. Chem. 78 (2) (2006) 379–386.
[83] The stable version of LAMMPS used here does not allow the implementation of a magnetic field. We thus use an electric field, which reproduces the same effect (torque) on the dipole moments. Note that this is possible only if no point charges are considered. For the units of the dipole moments and the external field see the LAMMPS manual https://docs.lammps.org/units.html, where the value of ε_0 is replaced with μ_0^{-1}.
[84] E. Atefi, J.A. Mann Jr., H. Tavana, Ultralow interfacial tensions of aqueous two-phase systems measured using drop shape, Langmuir 30 (32) (2014) 9691–9699.
[85] J. Brader, R. Evans, The fluid-fluid interface of a model colloid-polymer mixture, Europhys. Lett. 49 (5) (2000) 678.
[86] A.L. Grilo, M. Raquel Aires-Barros, A.M. Azevedo, Partitioning in aqueous two-phase systems: fundamentals, applications and trends, Sep. Purif. Rev. 45 (1) (2016) 68–80.
[87] Y.K. Yau, C.W. Ooi, E.-P. Ng, J.C.-W. Lan, T.C. Ling, P.L. Show, Current applications of different type of aqueous two-phase systems, Bioresour. Bioprocess. 2 (1) (2015) 1–13.